American Mineralogist, Volume 103, pages 1975–1980, 2018

High-pressure single-crystal structural analysis of $AlSiO_3OH$ phase egg

Kirsten Schulze[1,*], Martha G. Pamato[2], Alexander Kurnosov[1], Tiziana Boffa Ballaran[1], Konstantin Glazyrin[3], Anna Pakhomova[3], and Hauke Marquardt[1,4]

[1]Bayerisches Geoinstitut, University Bayreuth, 95440 Bayreuth, Germany
[2]Department of Earth Sciences, University College London, WC1E 6BT London, U.K.
[3]FS-PE, Deutsches Elektronen Synchrotron, Hamburg 22607, Germany
[4]Department of Earth Sciences, University of Oxford, OX1 3AN Oxford, U.K.

Abstract

We present the first equation of state and structure refinements at high pressure of single-crystal phase egg, $AlSiO_3OH$. Phase egg is a member of the Al_2O_3-SiO_2-H_2O system, which contains phases that may be stable along a typical mantle geotherm (Fukuyama et al. 2017) and are good candidates for water transport into Earth's deep mantle. Single-crystal synchrotron X-ray diffraction was performed up to 23 GPa. We observe the **b** axis to be the most compressible direction and the β angle to decrease up to 16 GPa and then to remain constant at a value of ~97.8° up to the maximum experimental pressure reached. Structure refinements performed at low pressures reveal a distorted octahedron around the silicon atom due to one of the six Si-O bond lengths being significantly larger than the other five. The length of this specific Si-O4 bond rapidly decreases with increasing pressure leading to a more regular octahedron at pressures above 16 GPa. We identified the shortening of the Si-O4 bond and the contraction of the vacant space between octahedral units where the hydrogen atoms are assumed to lie as the major components of the compression mechanism of $AlSiO_3OH$ phase egg.

Keywords: Phase egg, single-crystal, X-ray diffraction, compressibility, structure refinement

Introduction

Hydrous aluminosilicate phases show a larger temperature stability field than the respective Mg end-members and are expected to be stable along a typical geotherm (Fukuyama et al. 2017). Therefore, they are assumed to play an important role in the Earth's deep water cycle (Gatta et al. 2014; Pamato et al. 2015; Fukuyama et al. 2017). $AlSiO_3OH$ phase egg is stable within the transition zone (Sano et al. 2004; Fukuyama et al. 2017) and probably also in the upper lower mantle up to pressures of 26 GPa at 1460–1600 °C (Pamato et al. 2015). Nanocrystalline diamond inclusions with a 1:1 Al to Si composition were found, providing a direct indication for its existence within Earth's mantle (Wirth et al. 2007). $AlSiO_3OH$ phase egg was first synthesized by Eggleton et al. (1978), and its structure was first solved by Schmidt et al. (1998). Phase egg has a monoclinic structure with $P2_1/n$ space group (Fig. 1) and the ideal formula $AlSiO_3OH$ contains 7.5 wt% H_2O. The crystal structure is made up of columns of edge-shared octahedra corner linked to the other columns with hydrogen occupying the vacant space between columns (Schmidt et al. 1998) bonded to the O4 oxygen atoms. Vanpeteghem et al. (2003) performed an X-ray powder diffraction study on phase egg to a maximum pressure of 40 GPa at room temperature and described its compressibility using a third-order Birch-Murnaghan equation of state with a room-pressure bulk modulus $K_0 = 157(4)$ GPa and its pressure-derivative $K_0' = 6.5(4)$. This previous study has highlighted the anisotropic compression response of phase egg with the shortest unit-cell axis being the most compressible. Vanpeteghem et al. (2003) suggested that this behavior may be caused by a larger compression of some of the O-O distances, but they have not performed structural refinements at high pressure to support this hypothesis.

Here, we present the first single-crystal X-ray diffraction data on phase egg collected to a maximum pressure of 23 GPa at ambient temperature using neon as a pressure-transmitting medium. Our single-crystal data allows for the characterization of the structural evolution of phase egg with pressure and the clear identification of the compression mechanisms.

Methods

Sample synthesis and characterization

Phase egg single-crystals were synthesized at 26 GPa and 1600 °C in a 1000 t Kawai type multi-anvil apparatus at the Bayerisches Geoinstitut (BGI) (run number: S5050) using a mixture of Al_2O_3:$Al(OH)_3$:SiO_2 in a wt% ratio of 13.59:39.27:47.15 as starting composition. The run product resulted in a mixture of phase egg, Al-phase D, and Stishovite. Further details on the synthesis and characterization are given in Pamato et al. (2015). The chemical composition of phase egg as determined by microprobe analysis by Pamato et al. (2015) is $Al_{0.98(1)}Si_{0.92(1)}O_3OH_{1.39(5)}$.

A single-crystal with dimensions 28 × 77 × 42 μm³ that showed sharp diffraction profiles, with a full-width at half maximum in omega scans below 0.06°, was selected from the run product and measured at ambient conditions on a four-circle Huber diffractometer equipped with Mo$K\alpha$ radiation and a point detector at BGI. A total of 25 reflections between 15 and 40 in °2θ were centered using the eight-position centering method according to the procedure of King and Finger (1979) implemented in the SINGLE operating software (Angel and Finger 2011). The unit-cell lattice parameters were determined using vector-least-squares refinements (Table 1). Single-crystal X-ray diffraction measurements for structure refinement at ambient conditions were performed at BGI using an Oxford XCalibur diffractometer using Mo$K\alpha$ radiation ($\lambda = 0.70937$ Å) operated at 50 kV and 40 mA. The system is equipped with a graphite monochromator and a Sapphire 2 CCD area detector at a distance of 50.83 mm. Omega scans were

* E-mail: Kirsten.Schulze@uni-bayreuth.de

0003-004X/18/0012–1975$05.00/DOI: https://doi.org/10.2138/am-2018-6562

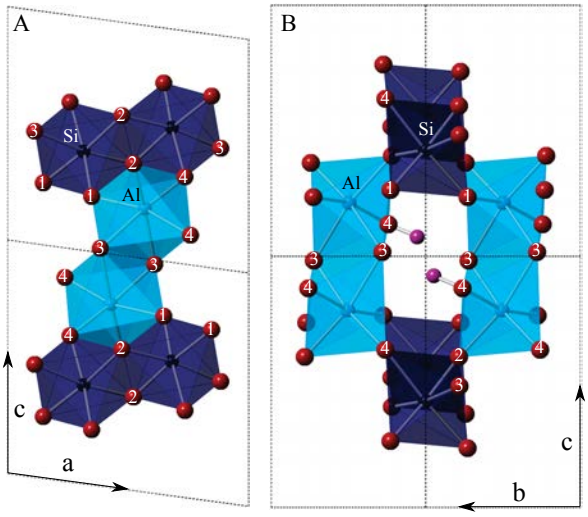

FIGURE 1. The structure of phase egg in the (010) and (100) plane. Silicon octahedra are shown in dark blue and aluminum octahedra are light blue. The oxygen atoms are marked red and labeled according to the nomenclature presented by Schmidt et al. (1998). The hydrogen atom (purple) positions are taken from Schmidt et al. (1998) and are situated in the empty channels. (Color online.)

TABLE 1. Unit-cell lattice parameters and volumes of phase egg collected at different pressures

P (GPa)	*a* (Å)	*b* (Å)	*c* (Å)	*V* (Å³)	β (°)
0.0001[a]	7.1835(2)	4.3287(2)	6.9672(2)	214.43(1)	98.201(2)
1.09(5)	7.1738(2)	4.3092(4)	6.9499(3)	212.69(2)	98.114(4)
1.82(5)	7.1666(2)	4.2977(3)	6.9375(2)	211.553(17)	98.080(3)
3.09(7)	7.1613(3)	4.2819(4)	6.9249(3)	210.28(2)	98.007(5)
4.15(8)	7.1505(4)	4.2632(7)	6.9107(5)	208.64(4)	97.953(8)
4.87(6)	7.1488(4)	4.2564(5)	6.9071(6)	208.14(3)	97.966(9)
6.92(9)	7.1267(4)	4.2357(5)	6.8801(6)	205.74(3)	97.853(9)
9.74(10)	7.1128(3)	4.2132(3)	6.8639(4)	203.78(2)	97.838(6)
11.67(9)	7.0951(6)	4.1968(6)	6.8456(7)	201.93(4)	97.842(11)
14.54(11)	7.0693(2)	4.1722(2)	6.8187(2)	199.252(12)	97.805(3)
16.82(11)	7.0533(2)	4.1583(2)	6.8029(3)	197.687(14)	97.793(4)
17.27(15)	7.0529(2)	4.1561(3)	6.8030(3)	197.567(17)	97.800(5)
18.56(13)	7.0424(4)	4.1452(4)	6.7950(5)	196.52(3)	97.814(8)
19.33(17)	7.0356(3)	4.1403(3)	6.7875(4)	195.886(19)	97.806(6)
21.44(18)	7.0263(3)	4.1302(4)	6.7774(5)	194.86(3)	97.799(8)
23.33(18)	7.0138(3)	4.1209(3)	6.7661(4)	193.75(2)	97.802(6)

Note: Numbers in parentheses refer to the uncertainty in the last given digit.
[a] Measured using the Huber diffractometer at BGI.

chosen to obtain a large redundancy of the reciprocal sphere up to $2\theta_{max} = 81°$. Frames were collected for 10 s using a step size of 0.5°. The CrysAlis package (Oxford Diffraction 2006) was used to integrate the intensity data taking into account both Lorentz and polarization factors as well as an empirical absorption correction. The observed reflections were consistent with the $P2_1/n$ space group, with a resulting discrepancy factor, R_{int}, of 0.055. Structure refinements based on F^2 were performed using the ShelX program (Sheldrick 2008) implemented in the WinGX system (Farrugia 2012). The atomic parameters reported by Schmidt et al. (1998) were used as starting parameters, and neutral scattering factors (Ibers and Hamilton 1974) were employed for Si, Al, and O. All atom positions were refined allowing for anisotropic displacement parameters. We performed structure refinements at ambient conditions with both fixed and refined occupancies for Si and Al in the two non-equivalent cation sites, respectively. Within uncertainties, the two models gave identical results for atomic positions and bond distances. The fully occupied model was therefore chosen for the following discussion. A total of 55 parameters were refined using 1348 unique reflections with resulting discrepancy factor $R1 = 0.054$. Atomic positions and displacement parameters are reported in the deposited[1] CIF.

High-pressure experiments

The phase egg single-crystal was loaded in a BX90 (Kantor et al. 2012) diamond-anvil cell (DAC) equipped with 350 μm culet sized diamonds. A 200 μm rhenium gasket was pre-indented to ~60 μm and a 200 μm hole was cut. Ruby spheres were added for in situ pressure determination. The gas-loading system installed at BGI (Kurnosov et al. 2008) was used to load neon at 1.5 kbar pressure as a pressure-transmitting medium.

High-pressure single-crystal X-ray diffraction was performed at the Extreme Conditions Beamline P02.2 at PETRA III at the Deutsches Elektronen Synchrotron (DESY). Intensity data were collected at 15 pressure points between 1.09 and 23.33 GPa using a focused monochromatic 0.2907 Å beam with a beam size of 2 × 4 μm² and a PerkinElmer area detector calibrated using a single-crystal of enstatite. Diffraction images were collected in omega scans between –34° to +34° in 1° steps with an exposure time of 1 s. The pressure in the cell was increased using a pressure membrane and measured from the ruby Raman fluorescence shift according to the calibration of Deweale et al. (2008). Data integration was performed using the CrysAlis package (Oxford Diffraction 2006). More than 520 reflections were used at all but two pressure points (120 and 371 reflections at 6.92 and 11.67 GPa, respectively) to determine the unit-cell lattice parameters reported in Table 1.

Structure refinements were performed at 10 different pressure points following the same procedure as used for the room-pressure intensity data. However, given the smaller number of unique reflections due to the restrictions imposed by the use of a DAC, the oxygen sites were refined isotropically. At each pressure point, the atomic positions of the previous pressure were used as starting parameters for the refinement. The number of unique reflections varied between 496 and 687 with R_{int} between 0.0246 and 0.1902, while the total number of parameters was reduced to 36. The resulting discrepancy factors, $R1$, ranged between 0.0405 and 0.1059. Details of the structural refinements, atomic positions, and displacement parameters are reported in the deposited[1] CIF.

RESULTS AND DISCUSSION

Compressibility of phase egg

The unit-cell lattice parameters of phase egg are shown in Figure 2 as a function of pressure and compared to literature data. No evidence for phase transitions can be observed in agreement with the results reported by Vanpeteghem et al. (2003). A plot of the normalized pressure F vs. the Eulerian strain f (Angel 2000) indicates that a third-order Birch-Murnaghan equation of state (EoS) is required to fit the P-V data (Supplemental[1] Fig. S1). The room-pressure unit-cell volume, V_0, the bulk modulus, K_0, and its pressure derivative, K_0', were refined using the software EoSFit7c (Angel et al. 2014) resulting in the following EoS parameters: $V_0 = 214.08(17)$ Å³, $K_0 = 153(8)$ GPa, and $K_0' = 8.6(1.3)$ (Table 2). Note that in the fitting procedure the unit-cell volume collected at room pressure was not considered to avoid biases due to the different techniques used (*in-house* diffractometer with point detector vs. synchrotron radiation with a two-dimensional detector).

The V_0 obtained in this study is larger than that measured in earlier studies (Schmidt et al. 1998; Vanpeteghem et al. 2003), but is in agreement with the unit-cell volume measured *in-house* at ambient conditions for our sample (Fig. 2a). The chemical analysis of our sample shows small deficiencies of silicon and aluminum, which we assume to be substituted by hydrogen to ensure charge balance. Schmidt et al. (1998) reported an Al:Si ratio close to unity and Vanpeteghem et al. (2003) assumed unity based on the nominal composition of the starting material used to synthesize phase egg. The presence of very small amounts of Al and Si vacancies in our sample, as well as the different synthesis conditions (i.e., higher pressure and temperature used in this study) and the different X-ray diffraction techniques used (single-crystal vs. powder diffraction), may explain the difference in unit-cell volumes among the three studies. Note, however,

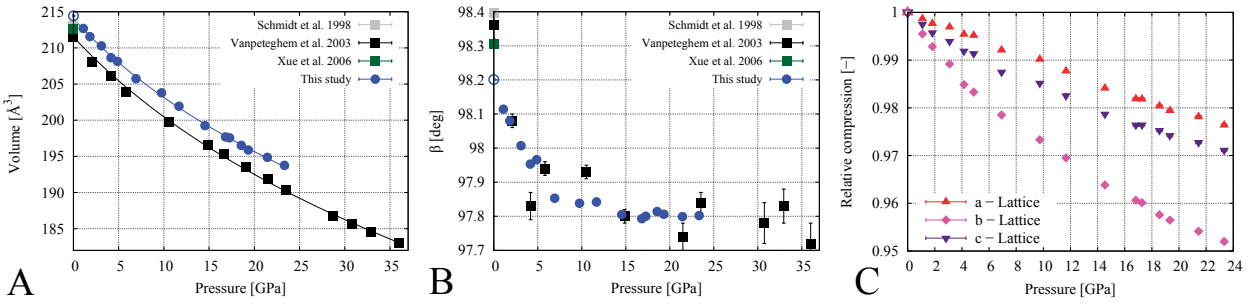

FIGURE 2. (**a**) Unit-cell volume, (**b**) β angle, and (**c**) relative unit-cell lattice parameters (a/a_0, b/b_0, and c/c_0) of phase egg. Open circles represent the room-pressure data measured in this study, whereas filled circles are results from the high-pressure measurements. The solid curves represent the third-order Birch-Murnaghan Equation of State fit. Literature data are shown for comparison (Schmidt et al. 1998; Vanpeteghem et al. 2003; Xue et al. 2006). Uncertainties are smaller or comparable to the symbol size unless error bars are shown. (Color online.)

TABLE 2. EoS parameters resulting from Birch-Murnaghan equation of state fits for both bulk and axial compressibilities of phase egg

	Vanpeteghem et al. (2003)		This study
	published	refitted	
V_0 (Å³)		211.41(11)	214.08(17)
K_0 (GPa)	157(4)	155(5)	153(8)
K'	6.5(4)	6.7(5)	8.6(1.2)
a_0 (Å)		7.136(6)	7.1848(12)
M_{a0} (GPa)		942(58)	833(14)
M'_a		12[a]	12[a]
b_0 (Å)		4.322(5)	4.327(2)
M_{b0} (GPa)		226(21)	240(16)
M'_b		25(3)	30(3)
c_0 (Å)		6.930(5)	6.963(2)
M_{c0} (GPa)		498(57)	497(40)
M'_c		32(7)	36(7)

Notes: The axial compressibilities from a previous powder diffraction experiment (Vanpeteghem et al. 2003) have been recalculated in this study. Numbers in parentheses refer to the uncertainty in the last given digit.
[a] Second-order Birch-Murnaghan EoS.

that the room-pressure crystal structure refinements performed here gave identical results within uncertainties when refining or fixing to unity the Al and Si occupancies. This implies that the effect of vacancies on the crystal structure of phase egg cannot be resolved in our structural model.

The K_0 obtained in this study is in agreement with that reported in the high-pressure powder diffraction study of Vanpeteghem et al. (2003) within uncertainties (Table 2). The pressure derivative determined in this study is instead larger than that reported by Vanpeteghem et al. (2003), resulting in lower compressibility of our sample at high pressure. However, the *F-f* plot constructed using the data reported by Vanpeteghem et al. (2003) (Supplemental[1] Fig. S2) reveals a kink at about 16 GPa with the lower-pressure data suggesting a much steeper slope than the higher-pressure data. Therefore, the value of K' reported by Vanpeteghem et al. (2003) is likely an average of these two clearly different compression behaviors. A change in compression mechanism is indeed suggested by the high-pressure variation of the β angle that shows a rapid decrease with pressure up to 16 GPa (Fig. 2b) but then remains practically constant at a value of ~97.8° up to the largest pressure reached both in this study and in the study of Vanpeteghem et al. (2003). This change in compression behavior is clearly more pronounced in the powder data since we do not observe a sharp kink in the *F-f* plot constructed with the data collected in this study. This is likely due to the different stress states present in the powder and in the single-crystal diamond-anvil cell experiments.

The variation with pressure of the unit-cell axes is very anisotropic as already suggested by Vanpeteghem et al. (2003). As can be seen from Figure 2c, the **b** axis is the most compressible direction, despite being the shortest of the three unit-cell parameters. Linearized Birch-Murnaghan EoS (Angel et al. 2014) was fitted to the data (Table 2). The linear modulus for the compression along the **b** axis is much lower than those along the other two axes (Table 2). Moreover, whereas the **a** axis can be fitted using a second-order Birch-Murnaghan EoS as the data plot on a horizontal line in a *F-f* plot (Angel 2000), both **b** and **c** axes have a very steep slope suggesting a larger stiffening of the phase egg structure with pressure along these two directions. To compare the axial compressibility obtained in this study with that obtained by Vanpeteghem et al. (2003), we have refitted the published data using the same linearized Birch-Murnaghan EoS, since in the mentioned study the axial behavior has been described using simple polynomials. Both **b** and **c** axes appear to have identical M_0 within the uncertainties. However, the **a** axis of the sample investigated in this study appears more compressible than that of the sample investigated by Vanpeteghem et al. (2003). Moreover, the polynomial variation with pressure of the **a** axis reported in Vanpeteghem et al. (2003) has a negative coefficient of the quadratic term, which implies that this direction becomes softer with increasing pressure. This further supports the hypothesis that the published data were obtained in a different stress environment with respect to that present in our experiment. Since we have not observed broadening of the single-crystal reflections up to the maximum pressure reached, we expect that the condition in our study was effectively hydrostatic.

In crystals with orthorhombic or higher symmetry, the changes of the unit-cell lattice parameters with pressure define the variation of the strain ellipsoid describing the distortion of the unstrained crystal with increasing pressure (Nye 1985). However, in the case of monoclinic and triclinic systems, unit-cell angles may also vary with pressure. Therefore the largest and smallest lattice changes in the crystal are not necessarily aligned parallel to the crystallographic axes.

The strain ellipsoid tensor components (Ohashi and Burnham 1973) for phase egg that has a monoclinic symmetry have been

calculated from the unit-cell lattice parameters at each pressure based on the Cartesian coordinate system with **X**||**a**, **Y**||**b**, and **Z**||**c*** according to the following equations:

$$e_{11} = \frac{a}{a_0} - 1 \quad e_{22} = \frac{b}{b_0} - 1 \quad e_{33} = \frac{c \sin\beta}{c_0 \sin\beta_0} - 1$$

$$e_{13} = \frac{1}{2}\left(\frac{c\cos\beta}{c_0 \sin\beta_0} - \frac{a\cos\beta_0}{a_0 \sin\beta_0} \right) \quad e_{12} = e_{23} = 0$$

where the zero denotes the room-pressure unit-cell parameters.

The principal strain components ε_{11}, ε_{22}, and ε_{33} and their orientation with respect to the crystallographic axes have been derived by diagonalization of the symmetrical strain tensor (Table 3). Due to the monoclinic symmetry, ε_{22} lies parallel to the **b** axis and has indeed the largest absolute values at all pressures indicating that this is the most compressible direction. The principal strain components ε_{11} and ε_{33} lie on the **a-c** plane, the former being the stiffer direction at ~30° (2) from **a** toward **c**. This direction is approximately perpendicular to the plane (904) and represents the direction along which columns of octahedra extend, having their shared edge perpendicular to this direction. The value of the unit strain (Hazen et al. 2000) in the stiffest direction, i.e., its fractional change per gigapascal remains invariant with pressure (Table 3), whereas the unit strain values in the other two directions, and especially that along the **b** axis, steadily decrease with pressure, implying that their compression significantly contribute to the pressure derivative of the bulk modulus. The orientation of the strain ellipsoid does not vary over the pressure range investigated in this study.

High-pressure structure

The individual octahedral bond distances for Si and Al are shown in Figure 3. At ambient pressures, the Si-O bond lengths are generally between 1.75 and 1.8 Å, with the exception of the Si-O4 bond that shows a value of about 2 Å in agreement with the study of Schmidt et al. (1998). At lower pressures, the coordination number of the silicon atom is, therefore, better described by 5+1.

A rapid reduction of the bond distance between the Si and the O4 atoms with pressure is clearly visible in Figure 3. The reduction between ambient conditions and the highest pressure point at 23.3 GPa is more than 9%, note, however, that the majority of this reduction has been already reached at ~16 GPa. Above this pressure, the Si octahedral coordination is much more regular, and the Si-O4 bond becomes as stiff as the other Si-O bond distances (Fig. 3). The Si-O4 bond contributes mainly to the compressions of the **b** and **c** axis. The stiffest Si-O bond is the Si-O3 that does not show any significant compression. All other Si octahedral bonds have similar compression rates, and their bond distances reduce by ~1.5–2% up to the highest pressure measured.

The compression of the Al octahedron is more uniform when compared to the Si octahedron, with two Al-O4 and one Al-O2 bond distances showing similar compressibilities, i.e., bond distance reductions between 3.7 and 4.4% in the studied pressure

TABLE 3. Principal strain components, their orientation with respect to the crystallographic axes, and the resulting unit strain components for the strain ellipsoid of phase egg

P (GPa)	ε_{11} 10^{-3}	ε_{22} 10^{-3}	ε_{33} 10^{-3}	ε_{11}^**a** (°)[a]	ε_{11}/GPa 10^{-3}	ε_{22}/GPa 10^{-3}	ε_{33}/GPa 10^{-3}
1.09(5)	−0.85(8)	−4.50(10)	−2.76(8)	30.7	−0.78	−4.13	−2.54
1.82(5)	−1.71(7)	−7.16(8)	−4.59(7)	28.0	−0.94	−3.93	−2.52
3.09(7)	−2.07(8)	−10.81(10)	−6.61(8)	28.4	−0.67	−3.50	−2.14
4.15(8)	−3.24(9)	−15.13(17)	−8.85(9)	29.5	−0.78	−3.65	−2.13
4.87(6)	−3.63(9)	−16.70(12)	−9.25(10)	27.6	−0.74	−3.43	−1.90
6.92(9)	−5.96(9)	−21.48(12)	−13.61(10)	30.4	−0.86	−3.10	−1.97
9.74(10)	−7.85(8)	−26.68(8)	−15.94(9)	29.8	−0.81	−2.74	−1.64
11.67(9)	−10.39(10)	−30.47(15)	−18.51(11)	29.1	−0.89	−2.61	−1.59
14.54(11)	−13.74(7)	−36.16(6)	−22.51(8)	29.7	−0.94	−2.49	−1.55
16.82(11)	−15.89(7)	−39.37(6)	−24.83(8)	30.0	−0.94	−2.34	−1.48
17.27(15)	−15.99(7)	−39.87(8)	−24.80(8)	30.0	−0.93	−2.31	−1.44
18.56(13)	−17.51(9)	−42.39(10)	−25.92(9)	30.3	−0.94	−2.28	−1.40
19.33(17)	−18.42(8)	−43.52(8)	−27.02(9)	30.2	−0.95	−2.25	−1.40
21.44(18)	−19.69(8)	−45.86(10)	−28.47(9)	30.0	−0.92	−2.14	−1.33
23.33(18)	−21.44(8)	−48.01(8)	−30.09(9)	30.2	−0.92	−2.06	−1.29

Note: Numbers in parentheses refer to the uncertainty in the last given digit.
[a] Angle between ε_{11} and **a** toward **c**.

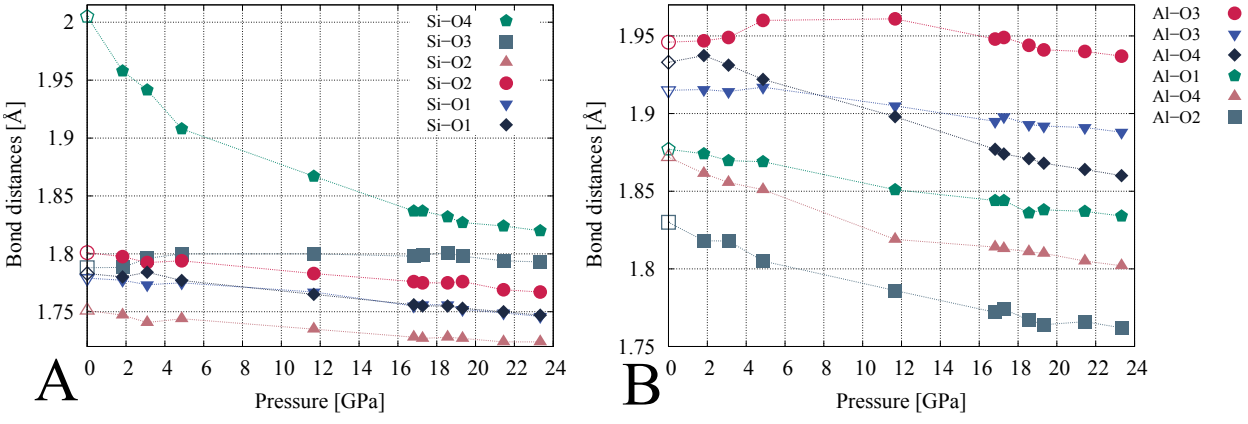

FIGURE 3. (**a**) Si-O individual bond distances. The Si-O4 bond is elongated at room pressure and is more compressible than all the other bonds. At pressures above 16 GPa, the silicon octahedron adopts a more regular shape and becomes stiffer. (**b**) Al-O individual bond distances. Open circles represent room-pressure data measured in this study, whereas filled circles are the high-pressure results from this study. Uncertainties are smaller or comparable to the symbol size. (Color online.)

range. The Al-O1 bond distance decreases by ~2.3% and one of the Al-O3 bond distances reduces by ~1.4% between room pressure and 23.3 GPa. The other Al-O3 bond distance shows practically no compression since the O3 atom connects the Si and the Al octahedron and forms the stiffest Si-O3 bond (Fig. 3).

The analysis of O-O distances reveals a more complicated compression mechanism than the simple picture suggested by Vanpeteghem et al. (2003). These authors indicated as a possible explanation for the large compressibility of the **b** axis the fact that the largest O-O distance lies in a direction nearly parallel to this axis as opposed to shorter O-O distances that are nearly parallel to the **a** and **c** directions. This reasoning is based on the assumption that longer distances are more compressible than shorter ones. However, this appears to be an invalid assumption in the case of phase egg, where the O-O distances involving the O4 atoms are most compressible independently from their value and direction. This is likely a consequence of the major compression of the Si-O4 bond. For example, the O4-O1 and O4-O2 distances that are perpendicular to the **b** direction (and therefore do not contribute to its compressibility) are relatively short but decrease by more than 4% in the pressure range investigated (Fig. 4), whereas the longer distance indicated by Vanpeteghem et al. (2003), which correspond in our study to the O4-O4 distance and contributes to the compressibility of the **b** direction, decreases only by ~3.8% (Fig. 4). As expected, the distances between the oxygen belonging to the shared octahedral edges are the least compressible and decrease less than 1% in the pressure range investigated, except for the O3-O4 shared edge that undergoes a 3.3% reduction between room pressure and 23.3 GPa (Fig. 4). Only one O-O distance shows a major compressibility, e.g., the O3-O3 distance between the columns of Al octahedra across the voids (Fig. 1b). This distance, which lies parallel to the **b** direction, decreases by more than 9% up to 23.3 GPa (Fig. 4) and is, therefore, responsible for the large compressibility of this axis.

IMPLICATIONS

Phase egg is a member of the Al_2O_3-SiO_2-H_2O system. In contrast to the Mg-Si end-member, the phases in the aluminum system are stable at temperatures of a typical mantle geotherm (Fukuyama et al. 2017). Phase egg and several other phases are therefore good candidates for water transport into the Earth's deep mantle through subduction of sediments and oceanic crust. Direct evidence for the occurrence of phase egg in the Earth's mantle came from the chemical composition of a diamond inclusion that showed a 1:1 Al to Si ratio and was assigned to phase egg (Wirth et al. 2007).

The most prominent feature in the high-pressure behavior of phase egg is the change in compression behavior of the Si-O4 bond in the Si-octahedron. Computational studies on the δ-AlOOH structure suggest that the compressibility of the structure is related to hydrogen bonding symmetrization (Tsuchiya et al. 2002). Based on this, Vanpeteghem et al. (2003) suggested that a stiffening of the H-O bonds could explain the curvature of the pressure dependence of the *b*-lattice parameter observed at high pressure for phase egg.

Schmidt et al. 1998 reported a position for the hydrogen atom that suggests an asymmetric O4-H···O3 configuration over the void space. Symmetrization and strengthening of

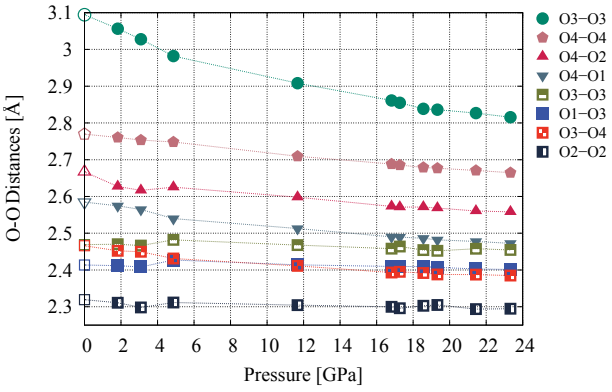

FIGURE 4. Selected oxygen–oxygen distances. The O3-O3 bond distance is measured across the voids between two columns of Al octahedra and shows the strongest reduction with pressure of all O–O distances. Squared symbols represent bonds involving octahedral shared edges. Open symbols represent room-pressure data measured in this study, whereas filled symbols are the high-pressure results from this study. Uncertainties are smaller or comparable to the symbol size. (Color online.)

similar configurations with increasing pressure were reported from computational calculations for diaspore (Friedrich et al. 2007) as well as from computational and experimental studies for iron oxyhydroxide (Xu et al. 2013). In diaspore the symmetrization of the hydrogen bonding and high compressibility along the void space is related to a strong compression of the donor-acceptor distance with increasing pressure. In phase egg the O3···O4 distance decreases from 2.608(1) Å at ambient pressure to 2.516(3) Å at 23.3 GPa. This represents a reduction of only 3.5% much smaller for example than the O3···O3 distance over the void space that reduces by about 9% in the same pressure range (Fig. 4). From our results, therefore, there is no evidence of symmetrization of the O4-H···O3 configuration in the pressure range where phase egg may be stable in the Earth's mantle. The Si-O4 bond distance is rapidly decreasing until 16 GPa pressure, strengthening the bond and weakening the O4-H bond. Thus, it is more likely that the regularization and further stiffening of the silicon octahedron is the reason for the change in compressional behavior above 16 GPa. Moreover, the high stability field to pressures and temperatures of the upper lower mantle of phase egg (Pamato et al. 2015) may be due to the decreasing distortion of the Si-octahedron that reaches a regular sixfold coordination.

ACKNOWLEDGMENTS

This research was supported through the project "GeoMaX" funded under the Emmy-Noether Program of the German Science Foundation (MA4534/3-1).

REFERENCES CITED

Angel, R.J. (2000) Equation of State. Reviews in Mineralogy and Geochemistry, 41, 35–59.

Angel, R.J., and Finger, L.W. (2011) SINGLE: a program to control single-crystal diffractometers. Journal of Applied Crystallography, 44, 247–251.

Angel, R.J., Alvaro, M., and Gonzales-Platas, J. (2014) EosFit7c and a Fortran module (library) for equation of state calculations. Zeitschrift für Kristallographie, 229, 405–419.

Deweale, A., Torrent, M., Loubeyre, P., and Mezouar, M. (2008) Compression curves of transition metals in the Mbar range: Experiments and projector augmented-wave calculations. Physical Review B, 78, 104102.

Eggleton, R.A., Boland, J.N., and Ringwood, A.E. (1978) High pressure synthesis of

a new aluminium silicate: $Al_5Si_5O_{17}(OH)$. Geochemical Journal, 12, 191–194.
Farrugia, L.J. (2012) WinGX and ORTEP for Windows: an update. Journal of Applied Crystallography, 45, 849–854.
Friedrich, A., Wilson, D.J., Haussühl, E., Winkler, B., Morgenroth, W., Refson, K., and Milman, V. (2007) High-pressure properties of diaspore, AlO(OH). Physics and Chemistry of Minerals, 34, 145–157.
Fukuyama, K., Ohtani, E., Shibazaki, Y., Kagi, H., and Suzuki, A. (2017) Stability field of phase egg, $AlSiO_3OH$ at high pressure and high temperature: possible water reservoir in mantle transition zone. Journal of Mineralogical and Petrological Sciences, 112, 31–35.
Gatta, G.D., Morgenroth, W., Dera, P., Petitgirard, S., and Liermann, H.-P. (2014) Elastic behavior and pressure-induced structure evolution of topaz up to 45 GPa. Physics and Chemistry of Minerals, 41, 569–577.
Hazen, R.M., Downs, R.T., and Prewitt, C.T. (2000) Principle of comparative crystal chemistry. Reviews in Mineralogy and Geochemistry, 41, 1–33.
Ibers, J.A., and Hamilton, W.C. (1974) International Tables for X-ray Crystallography, vol. IV. Kynoch, Birmingham, U.K.
Kantor, I., Prakapenka, V., Kantor, A., Dera, P., Kurnosov, A., Sinogeikin, S., Dubrovinskaia, N., and Dubrovinsky, L. (2012) BX90: A new diamond anvil cell design for X-ray diffraction and optical measurements. Review of Scientific Instruments, 83, 125102.
King, H.E., and Finger, L.W. (1979) Diffracted beam crystal centering and its application to high-pressure crystallography. Journal of Applied Crystallography, 12, 374–378.
Kurnosov, A., Kantor, I., Boffa-Ballaran, T., Lindhardt, S., Dubrovinsky, L., Kuznetsov, A., and Zehnder, B.H. (2008) A novel gas-loading system for mechanically closing of various types of diamond anvil cells. Review of Scientific Instruments, 79, 045110.
Nye, J.F. (1985) Physical Properties of Crystals: Their Representation by Tensors and Matrices, 352 p. Oxford University Press.
Ohashi, Y., and Burnham, C.W. (1973) Clinopyroxene lattice deformations: The role of chemical substitution and temperature. American Mineralogist, 58, 843–849.
Pamato, M.G., Myhill, R., Boffa Ballaran, T., Frost, D.J., Heidelbach, F., and Miyajima, N. (2015) Lower-mantle water reservoir implied by the extreme stability of a hydrous aluminosilicate. Nature Geoscience, 8, 75–79.
Sano, A., Ohtani, E., Kubo, T., and Funakoshi, K. (2004) In situ X-ray observation of decomposition of hydrous aluminum silicate $AlSiO_3OH$ and aluminum oxide hydroxide d-AlOOH at high pressure and temperature. Journal of Physics and Chemistry of Solids, 65, 1547–1554.
Schmidt, M.W., Finger, L.W., Angel, R.J., and Dinnebier, R.E. (1998) Synthesis, crystal structure, and phase relations of $AlSiO_3OH$, a high-pressure hydrous phase. American Mineralogist, 83, 881–888.
Sheldrick, G.M. (2008) A short history of SHELX. Acta Crystallographica, A64, 112–122.
Tsuchiya, J., Tsuchiya, T., Tsuneyuki, S., and Yamanaka, T. (2002) First principles calculation of a high-pressure hydrous phase, δ-AlOOH. Geophysical Research Letters, 29. 1909
Vanpeteghem, C.B., Ohtani, E., Kondo, T., Takemura, K., and Kikegawa, T. (2003) Compressibility of phase Egg $AlSiO_3OH$: Equation of state and role of water at high pressure. American Mineralogist, 88, 1408–1411.
Wirth, R., Vollmer, C., Brenker, F., Matsyuk, S., and Kaminsky, F. (2007) Inclusions of nanocrystalline hydrous aluminium silicate "phase egg" in superdeep diamonds from Juina (Mato Grosso State, Brazil). Earth and Planetary Science Letters, 259, 384–399.
Xu, W., Greenberg, E., Rozenberg, G.K., Pasternak, M.P., Bykova, E., Boffa Ballaran, T., Dubrovinsky, L., Prakapenka, V., Hanfland, M., Vekilova, O.Y., Simak, S.I., and Abrikosov, I.A. (2013) Pressure-induced hydrogen bond symmetrization in iron oxyhydroxide. Physical Review Letters, 111, 175501.
Xue, X., Kanzaki, M., Fukui, H., Ito, E., and Hashimoto, T. (2006) Cation order and hydrogen bonding of high-pressure phases in the Al_2O_3-SiO_2-H_2O system: An NMR and Raman study. American Mineralogist, 91, 850–861.

Manuscript received March 21, 2018
Manuscript accepted September 7, 2018
Manuscript handled by G. Diego Gatta

Endnote:

[1]Deposit item AM-18-126562, Supplemental figures and CIF. Deposit items are free to all readers and found on the MSA web site, via the specific issue's Table of Contents (go to http://www.minsocam.org/MSA/AmMin/TOC/2018/Dec2018_data/Dec2018_data.html).